Volume 26
Number 3
21 January 2024
Pages 1467–2706

PCCP

Physical Chemistry Chemical Physics

rsc.li/pccp

25 YEARS ANNIVERSARY

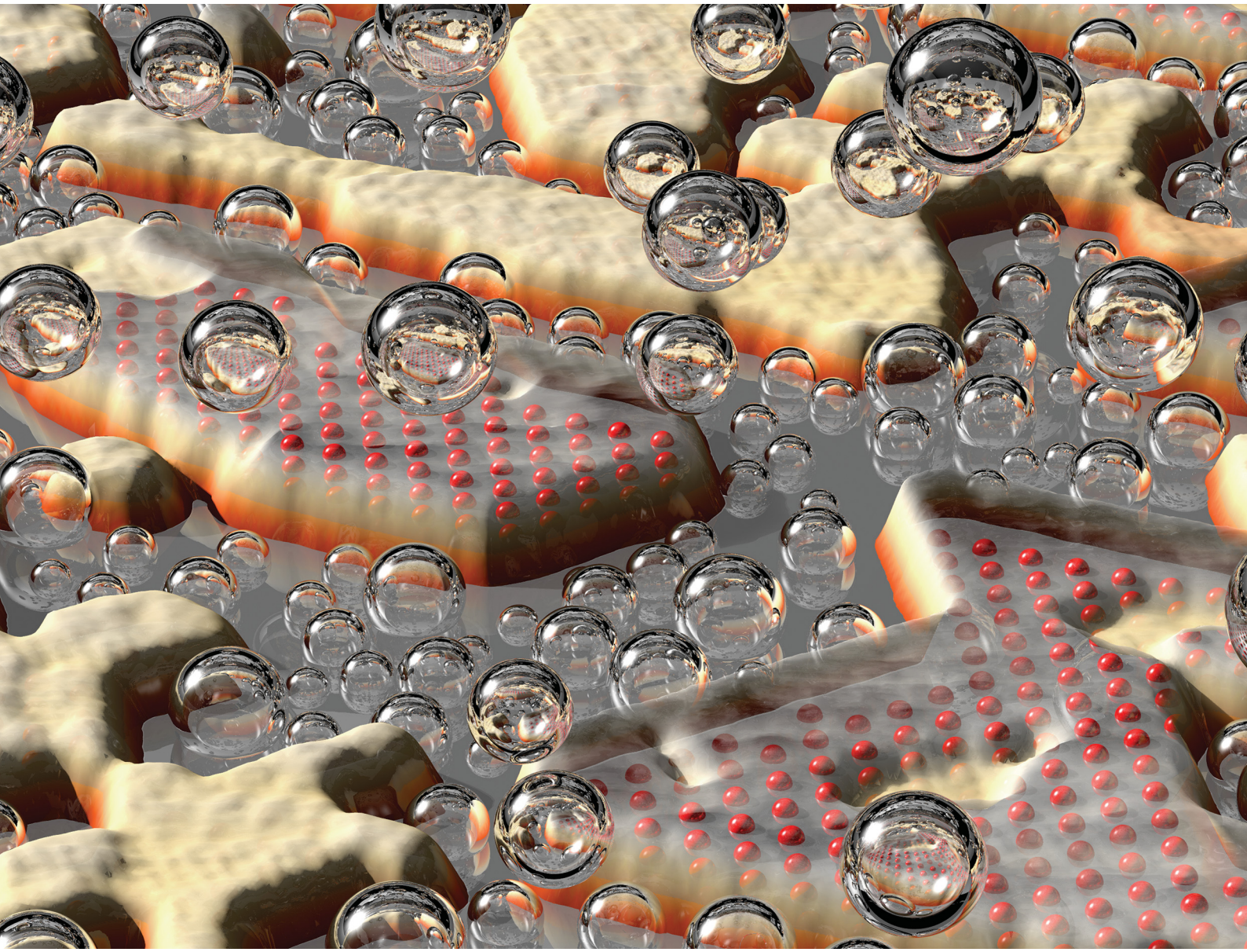

ISSN 1463-9076

ROYAL SOCIETY OF CHEMISTRY

PAPER

Olaf Brummel, Josef Mysliveček *et al.*
A model study of ceria–Pt electrocatalysts: stability, redox properties and hydrogen intercalation

PCCP Owner Societies

PCCP

ROYAL SOCIETY OF CHEMISTRY

PAPER

View Article Online
View Journal | View Issue

Cite this: *Phys. Chem. Chem. Phys.*, 2024, **26**, 1630

A model study of ceria–Pt electrocatalysts: stability, redox properties and hydrogen intercalation†

Lukáš Fusek, [ab] Pankaj Kumar Samal, [a] Jiří Keresteš,[a] Ivan Khalakhan, [a] Viktor Johánek, [a] Yaroslava Lykhach, [b] Jörg Libuda, [b] Olaf Brummel *[b] and Josef Mysliveček *[a]

The electrocatalytic properties of advanced metal-oxide catalysts are often related to a synergistic interplay between multiple active catalyst phases. The structure and chemical nature of these active phases are typically established under reaction conditions, *i.e.* upon interaction of the catalyst with the electrolyte. Here, we present a fundamental surface science (scanning tunneling microscopy, X-ray photoelectron spectroscopy, and low-energy electron diffraction) and electrochemical (cyclic voltammetry) study of CeO_2(111) nanoislands on Pt(111) in blank alkaline electrolyte (0.1 M KOH) in a potential window between −0.05 and 0.9 V_{RHE}. We observe a size- and preparation-dependent behavior. Large ceria nanoislands prepared at high temperatures exhibit stable redox behavior with Ce^{3+}/Ce^{4+} electrooxidation/reduction limited to the surface only. In contrast, ceria nanoislands, smaller than ∼5 nm prepared at a lower temperature, undergo conversion into a fully hydrated phase with Ce^{3+}/Ce^{4+} redox transitions, which are extended to the subsurface region. While the formation of adsorbed OH species on Pt depends strongly on the ceria coverage, the formation of adsorbed H_{ads} on Pt is independent of the ceria coverage. We assign this observation to intercalation of H_{ads} at the Pt/ceria interface. The intercalated H_{ads} cannot participate in the hydrogen evolution reaction, resulting in the moderation of this reaction by ceria nanoparticles on Pt.

Received 10th August 2023,
Accepted 3rd October 2023

DOI: 10.1039/d3cp03831a

rsc.li/pccp

Introduction

Understanding the catalytic properties of advanced electrocatalysts for energy conversion and storage requires detailed characterization of the catalyst–electrolyte interface under operating conditions. Upon contact with the electrolyte at operating potential, the as-prepared electrocatalysts undergo structural and chemical changes yielding active catalyst phases.[1,2] These changes may include the hydration and hydroxylation of the catalyst surfaces,[3–5] leaching of electrochemically unstable species,[6,7] or structural transformations.[8,9] In specific cases, electrochemical activities of a broad spectrum of the as-prepared catalysts can be traced back to a considerably narrower range of electrochemically active phases. A representative example is the formation of transition metal oxyhydroxides on the surface of various transition metal compounds during water electrolysis.[10] Combining multiple electrochemically active phases can yield new reaction pathways and increase significantly the activity of the catalyst, as shown for noble and transition metal-based electrocatalysts activated with transition metal compounds.[11–13]

The complex nature of real high-area electrocatalysts[1,2] and their interaction with electrolytes underlines the importance of model approaches which utilize well-defined model systems. In such model studies, quantitative information on the stability and catalytic activity can be obtained with atomic resolution on single crystalline, thin film or nanoparticulate samples combining experimental approaches of surface science and electrochemistry.[14–18] The importance of transition metal-based catalysts for alkaline water electrolysis is fueling current interest in model electrocatalytic studies predominantly on Co, Fe, and Ni oxides and oxyhydroxides. Model studies reveal the formation of active hydroxylated phases,[19–21] the stability of electrocatalyst surfaces under operating conditions,[22–25] and activation of electrocatalysts *via* doping[26–28] or bifunctional interactions in the presence of noble metals.[19,29]

[a] *Charles University, Faculty of Mathematics and Physics, Department of Surface and Plasma Science, V Holešovičkách 2, 180 00 Praha 8, Czech Republic. E-mail: josef.myslivecek@mff.cuni.cz*
[b] *Interface Research and Catalysis, Friedrich-Alexander-Universität Erlangen-Nürnberg, Egerlandstr. 3, 91058 Erlangen, Germany. E-mail: olaf.brummel@fau.de*

† Electronic supplementary information (ESI) available. See DOI: https://doi.org/10.1039/d3cp03831a

Here, we present a model electrocatalytic study on a specific class of catalytically relevant oxides – rare earth oxides, as represented by cerium oxide (ceria). Apart from its wide application in heterogeneous catalysis,[30,31] ceria finds promising applications in electrocatalysis mainly as a co-catalyst for activation of ammonia, alcohol, and CO electrooxidation,[32–34] and for reactions related to electrolysis and fuel cells – the hydrogen evolution reaction (HER),[35] oxygen reduction reaction (ORR),[36–38] and oxygen evolution reaction (OER).[39] Ceria-based electrocatalysts are generally synthesized in the form of cerium oxide[32–38] or cerium hydroxide[39] nanoparticles, interfacing nanoparticles of a second catalytically active phase – metal[32–38] or metal oxyhydroxide.[39] The heterogeneous interface between the catalytically active phases is, correspondingly, identified as the source of improvement of ceria-based electrocatalyst properties *via* charge transfer between a metal and ceria,[32,36,37,39] enhanced water dissociation and OH supply,[33,35] or *via* formation of specific defects in ceria.[37,38] The enhancement of the ceria-based electrocatalyst properties can be co-determined by the size and structure of the ceria nanoparticles.[32,38] All the above-mentioned synergistic effects of ceria in ceria-based electrocatalysts must critically depend on the nature of the cerium phases established under electrochemical conditions. These, however, have remained largely unknown so far.

To obtain elementary information on the nature of the cerium phases under electrochemical conditions, we investigate the stability and electrochemical reduction/oxidation properties of CeO_2(111) nanoislands prepared on Pt(111) in alkaline electrolyte (0.1 M KOH). The properties of the as-prepared and electrochemically treated ceria/Pt model catalysts are quantified using experimental methods of surface science – scanning tunneling microscopy (STM), X-ray photoelectron spectroscopy (XPS), low-energy electron diffraction (LEED), and atomic force microscopy (AFM), in combination with cyclic voltammetry (CV). We use different preparation methods to obtain samples with varying lateral sizes of ceria nanoislands. We collect evidence for hydration of ceria nanoislands smaller than 5 nm, and the corresponding surface or subsurface Ce^{3+}/Ce^{4+} electrooxidation/reduction of large CeO_2(111) and small $CeO_2 \cdot 2H_2O$ nanoislands, respectively. An evaluation of ceria coverage, in comparison with the charges assigned to Ce^{3+}/Ce^{4+} transition and to H and OH adsorption/desorption on Pt(111), indicates reversible intercalation of adsorbed H_{ads} at the ceria/Pt interface. The intercalated H_{ads} is unable to participate in the hydrogen evolution reaction (HER).

Results and discussion

Preparation and characterization of the samples by surface science methods

Samples of ceria–Pt electrocatalysts were prepared by means of physical vapor deposition in the form of inverse model catalysts consisting of CeO_2(111) nanoislands supported on Pt(111). The samples were prepared using two methods which yielded distinctly different CeO_2(111) nanoisland morphologies. The methods differed in thermal treatments during deposition and post-deposition, and are denoted as high-temperature (HT, final annealing temperature 1050 K) and low-temperature (LT, final annealing temperature 850 K) methods. Detailed description of the experimental procedures is given in the Materials and methods section of the ESI.† Samples with the amounts of deposited CeO_2 of approximately 1, 2, and 3 monolayers (ML) were prepared using both methods. STM images of the as-prepared samples are shown in Fig. 1. In the following discussion, 1 ML represents a basic O–Ce–O repeat unit of CeO_2(111) containing 7.9×10^{14} cm^{-2} Ce atoms, twice that of O atoms, and featuring a thickness of 3.1 Å.[30,31]

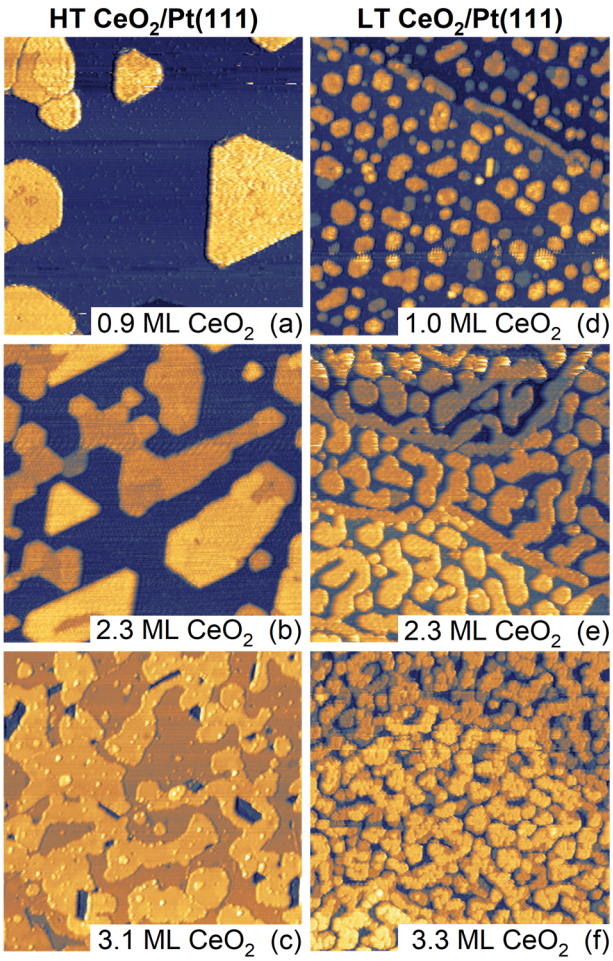

Fig. 1 STM images (150 × 150 nm^2) of CeO_2/Pt(111) samples prepared using two different methods. High temperature preparation (HT, final annealing at 1050 K) yields compact CeO_2(111) islands with straight edges (a)–(c). Low temperature preparation (LT, final annealing at 850 K) yields open CeO_2(111) islands with rounded edges, and a characteristic size <5 nm (d)–(f). Samples were prepared using the amounts of deposited CeO_2 of approximately 1 (a), (d), 2 (b), (e), and 3 monolayers (ML, (c) and (f)).

HT samples (Fig. 1a–c) exhibit a flat geometry and compact island shapes with straight edges aligned along high-symmetry substrate directions. With increasing amount of deposited CeO_2(111), the nanoislands extend laterally and coalesce to an almost continuous CeO_2(111) thin film for 3 ML of deposited

ceria (Fig. 1c). The growth of the ceria nanoislands resembles a layer-by-layer growth and is consistent with previous observations of CeO_2(111) growth on Pt(111).[40,41] The LEED diffraction pattern shows diffraction spots of the clean Pt(111) substrate and unreconstructed CeO_2(111) (Fig. S1a, ESI†). The LT samples (Fig. 1d–f) exhibit a similarly flat geometry but with distinctly smaller ceria nanoisland sizes compared to HT samples (Fig. 1d). With increasing amount of deposited ceria, coalescence yields open island shapes with rounded edges (Fig. 1e), and coalescence proceeds at a slower rate as compared to the HT samples (Fig. 1f). The round edges of the LT samples are expected to contain an increased amount of kink sites compared to the straight step edges of HT samples. Similar to HT samples, LT samples show a LEED pattern corresponding to CeO_2(111) on Pt(111) (Fig. S1b, ESI†). The effect of lowering the final annealing temperature on the morphology of LT samples is similar to previous observations of CeO_2(111) growth on Pt(111).[40,41]

Based on the STM images, we can quantify the evolution of morphological features of the HT and the LT samples as a function of the amount of deposited ceria. The results are summarized in Fig. S2 and Table S1 (ESI†). For both the HT and the LT samples, the coverage of the CeO_2(111) layer as determined by STM (θ^{Ce}_{STM}) scales linearly with the amount of deposited ceria, yielding a thickness of the CeO_2(111) nanoislands (4 ± 1) ML for all samples shown in Fig. 1. A distinct difference between the HT and the LT samples is the different lateral size of the CeO_2(111) structures, as identified by autocorrelation length obtained from the STM images (Fig. S2a, ESI†). The autocorrelation length of the LT samples is almost constant, reflecting the characteristic width of the CeO_2(111) structures ($\sim$5 nm), much smaller than the characteristic lateral size of HT CeO_2(111) nanoislands ($\sim$20 nm). The HT and the LT samples differ in the length of the metal-oxide boundary. For HT samples, the metal-oxide boundary amounts to 1–3% of the Pt(111) surface sites, while for the LT samples, the value is 5–7% (Fig. S2b, ESI†).

In addition to morphological differences, XPS reveals differences in the chemical state of the as-prepared HT and LT samples. This, particularly the concentration of Ce^{3+} species, is determined from the Ce 3d spectrum (Fig. S2c, ESI†). HT and LT samples show Ce^{3+} concentrations in the range of 4–8% and 12–16%, respectively. This corresponds, formally, to 1–2% and 3–4% O vacancy concentration relative to stoichiometric CeO_2 for HT and LT samples, respectively. The increased concentration of Ce^{3+} in the LT samples can be attributed to an increased concentration of structural defects (step edges, kinks) and oxygen vacancies as compared to the HT samples.

Electrochemical characterization of the samples

After preparation and characterization by surface science methods in an ultra-high vacuum (UHV), the ceria/Pt model catalysts were transferred through air into an electrochemical cell and characterized by CV in alkaline electrolyte (0.1 M KOH electrolyte, purged with Ar). All measurements were performed at potentials ranging from -0.05 to 0.9 V_{RHE} [potential *versus* the reversible hydrogen electrode (RHE)], and at a scan rate of 400 mV s^{-1}. An overview of the CV results for the HT and LT samples is presented in Fig. 2 and 3.

In Fig. 2, the CV of clean Pt(111) is presented for comparison. A detailed view of the clean Pt(111) reference as obtained in our experiments is presented in Fig. S3 (ESI†). The CV consists of three distinct regions: The hydrogen region (H desorption/adsorption) between -0.05 and 0.35 V_{RHE}, the double layer region between 0.35 and 0.65 V_{RHE}, and the oxygen region (OH adsorption/desorption) between 0.65 and 0.90 V_{RHE}. The total integrated charges associated with these regions $q^{ref}_{H/Pt}$ = 350 μC cm^{-2}, q^{ref}_{DL} =125 μC cm^{-2}, and $q^{ref}_{OH/Pt}$ = 305 μC cm^{-2} for the hydrogen, double layer, and oxygen region, respectively, are in good agreement with values reported in the literature.[15]

Fig. 2a and b show CVs of HT samples shown in Fig. 1a–c, and CVs of LT samples shown in Fig. 1 d–f, respectively. Both figures illustrate the dependence of the CV shape on the amount of deposited CeO_2. Compared to the CV of clean Pt(111), CVs of HT samples include a new pair of irreversible peaks positioned in the hydrogen region. CVs of LT samples include a new pair of irreversible peaks as well, however, it is positioned at higher potential (by approx. 0.3 V) in the double layer region of clean Pt(111). The features observable on Pt(111), corresponding to H desorption/adsorption, the double layer, and the OH adsorption/desorption, are clearly resolved for all samples. Qualitatively, for both the HT and the LT samples, the areas of the irreversible peaks increase with increasing amount of deposited ceria, while areas of the OH adsorption/desorption on Pt(111) decrease. The area of H desorption/adsorption on Pt(111) does not show apparent changes.

CVs in Fig. 2 represent stabilized CVs obtained upon immersion of the sample in the electrolyte and application of approx. 25 cycles. CVs obtained immediately after the immersion of the samples in the electrolyte are shown in Fig. 3. Fig. 3a illustrates that the CVs of the HT samples are stable from the first complete cycle, and remain stable on the time scale of the present experiments ($\sim$10 min contact of the samples with the electrolyte, $\sim$50 CV cycles). In contrast, distinct changes are observable in the shape of the CVs of the LT samples. Initially, irreversible peaks similar to the peaks of HT samples appear in the H adsorption/desorption region of Pt(111). These peaks, however, are quickly replaced by a pair of irreversible peaks localized at higher potentials. CVs with irreversible peaks in the double layer region stabilize within $\sim$20 cycles.

Assignment of the CV peaks

The irreversible peaks in the CVs of both HT and LT samples can be assigned to particular Ce phases as follows: At pH = 13, corresponding to the 0.1 M KOH electrolyte, the solubility of Ce^{3+} ions is negligible[42] and electrochemical phase transitions are expected to occur between hydroxylated phases, and, in the presence of oxygen (or traces of oxygen, such as in the Ar-saturated electrolytes), oxidized solid ceria phases.[43] In chemical compounds, Ce adopts exclusively Ce^{3+} and Ce^{4+} oxidation states,[30] and Ce^{3+} and Ce^{4+} oxidation states are also the only states considered in aqueous electrolytes under potential.[43] The observed irreversible peaks in both HT and LT CVs thus

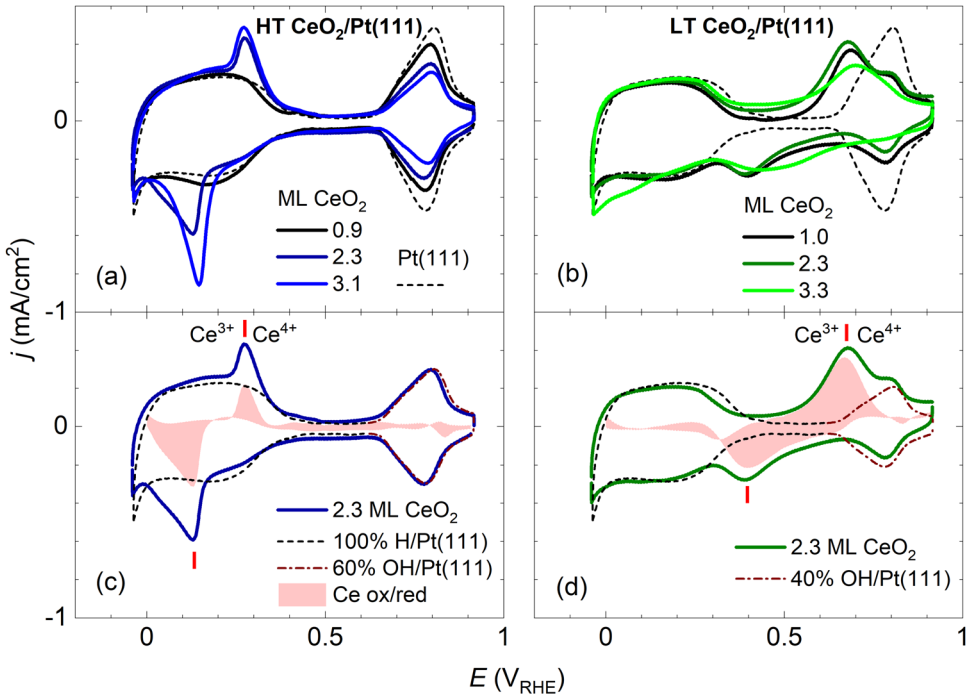

Fig. 2 Dependence of the stable CVs on the amount of deposited CeO_2 for HT samples shown in Fig. 1a–c (a), and for LT samples shown in Fig. 1d–f (b). For reference, the CV of clean Pt(111) is shown. Determination of the faradaic contribution to Ce^{3+}/Ce^{4+} electrooxidation/reduction for HT (c) and LT (d) samples. The red shaded area represents a difference between the experimental CV of a ceria/Pt sample (solid line) and scaled reference data for clean Pt(111). The red ticks indicate the positions of Ce^{3+}/Ce^{4+} redox peaks. CVs in 0.1 M KOH, at a scan rate of 400 mV s^{-1}.

correspond to Ce^{3+}/Ce^{4+} redox transitions. At pH =13, and potentials >0.7 V_{RHE} (highest-potential irreversible peak in our observations, Fig. 2b and d), Ce^{4+} containing phases must dominate.[43] The observed shift of the irreversible peaks by $\sim$0.3 V between HT and LT samples however indicates that the Ce^{4+} containing phases in the HT and LT samples are distinctly different.

The Ce phase present in a vacuum, under ambient conditions, and in water-based electrolytes is predominantly the cubic phase of CeO_2 which is observed across the whole range of ceria oxygen deficiency between CeO_2 and Ce_2O_3.[44–46] In the presence of water, the reduced cubic phase CeO_{2-x} can become partly hydroxylated.[31,45,47] At strong oxygen deficiency and in the presence of water, CeO_{2-x} thin films or nanoparticles are observed to convert to hexagonal $Ce(OH)_3$.[47–50] Finally, for highly dispersed CeO_2 powders, the amorphous hydrated phase with a stoichiometry of $CeO_2{\cdot}2H_2O$, also denoted as $Ce(OH)_4$, has been identified.[45,51,52] Given the properties of the known Ce phases, the HT and LT samples at oxidizing potentials >0.7 V_{RHE} are expected to consist of cubic CeO_2 or amorphous $CeO_2{\cdot}2H_2O$ phases, respectively.

The assignment of the redox transitions on the CeO_2 phase of the HT samples to Ce^{3+}/Ce^{4+}can be verified by recording a CV of a continuous thin film of CeO_2(111) on Pt(111) (see Fig. S4, ESI†). The CV of the continuous film does not show the peaks characteristic of clean Pt(111) and is dominated by a pair of irreversible peaks at potentials comparable to those observed on the HT samples (*cf.* Fig. 2). The CV of the continuous film corresponds well to previous observations on polycrystalline CeO_2 films.[53] Assignment of redox transitions observed on the LT samples to the Ce^{3+}/Ce^{4+} couple of hydrated $CeO_2{\cdot}2H_2O$ is supported by following indirect evidence: The initial instability of the CV on LT samples can be assigned to a progressive hydration of the as-prepared CeO_2(111) nanoislands during cycling. Similar as for the case of unsupported ceria nanoparticles,[45,51,52] hydration is observed only for ceria nanoislands with sizes smaller than $\sim$5 nm, *i.e.* for the LT samples. Finally, the mutual shift of the irreversible peaks in the CVs of HT and LT samples corresponds well to phase transitions predicted for ceria phases in water-based electrolytes, where the redox potential of hydrated ceria $CeO_2{\cdot}xH_2O \rightleftharpoons Ce(OH)_3$ at pH = 13 is found to be $\sim$0.3 V higher than the one of anhydrous ceria $CeO_2 \rightleftharpoons Ce(OH)_3$.[43]

Characterization of samples after electrochemical treatment

After finishing the CV experiments, the samples were taken out of the electrolyte under potential control at $\geq$0.75 V_{RHE}, ensuring that the oxidized character of both the LT and the HT samples is preserved. Samples were further examined *via* AFM in air and *via* XPS. AFM images of the samples indicate that the coverage, the flat character, and the compact shape of ceria nanoislands in HT samples are conserved during CV experiments (Fig. S5a–d, ESI†). For the LT samples (Fig. S5e–h, ESI†), the morphology of ceria and the distribution of ceria on the substrate are altered. These observations are in agreement with the electrochemical stability observed for the as-prepared HT samples (Fig. 3a), and with the transformation to hydrated $CeO_2{\cdot}2H_2O$ observed for the LT samples (Fig. 3b). A more detailed analysis of the AFM images is hampered by high noise level and

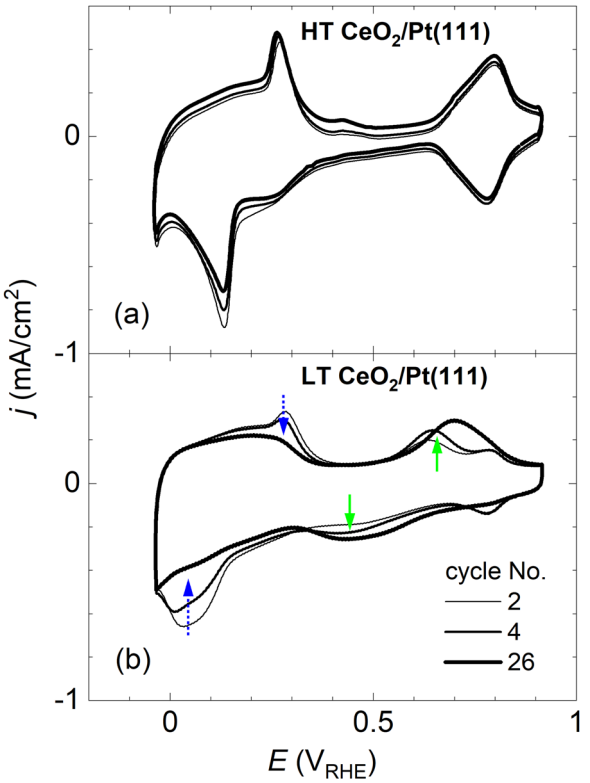

Fig. 3 Stability of the CVs upon immersion of the samples into the electrolyte. The representative HT sample in (a), and the LT sample in (b). In (b), the dotted arrows indicate disappearing peaks, and the full arrows indicate growing peaks. CVs in 0.1 M KOH, at a scan rate of 400 mV s^{-1}.

sample contamination during the manipulation of samples in air. XPS analysis of Ce 3d spectra on the HT samples after the CV experiments shows no changes with respect to the as-prepared state (Fig. S6a and b, ESI†), indicating a low concentration of structural defects and oxygen vacancies, supporting our assumption that the HT samples are stable under electrochemical conditions. In contrast, we observed reduction of ceria after the CV experiments for the LT samples (increase of Ce^{3+} fraction from 15 to 23%, Fig. S6c and d, ESI†). Reduction is observed in spite of several hour exposure of LT samples to air under ambient conditions prior to the XPS measurement. This may reflect an increased disorder or a partly hydroxylated nature of the LT samples after finishing the CV experiments. Both in air, and in the water-based solutions, amorphous nanoparticles of hydrated $CeO_2{\cdot}2\ H_2O$ were previously reported to convert spontaneously to a defect-rich, highly reduced cubic CeO_{2-x} phase.[45,51] Poor control over water exposure and carbon contamination during the manipulation of model catalyst samples in air did not allow a systematic investigation of the O 1s and C 1s XPS signals after the CV experiments.

Faradaic charges in the CV experiments of the HT and LT samples

We attempted to determine the charges related to the faradaic processes in the CV of the HT and LT samples, in particular the charge corresponding to Ce^{3+}/Ce^{4+} transition q_{Ce}, the charge corresponding to H adsorption/desorption on Pt(111) $q_{H/Pt}$, and the charge corresponding to OH adsorption/desorption on Pt(111) $q_{OH/Pt}$. Our estimate of the charges is based on the following CV features characteristic for both HT and LT samples:

(i) The presence of ceria nanoislands blocks the OH adsorption on the Pt(111) surface which results in decreasing $q_{OH/Pt}$. This effect is clearly visible in HT samples (Fig. 2a), where the OH adsorption/desorption peaks do not overlap with the Ce^{3+}/Ce^{4+} redox peaks. This effect is apparent in LT samples as well (Fig. 2b), where OH adsorption/desorption and Ce^{3+}/Ce^{4+} redox peaks are still clearly separated in the cathodic scan (Fig. 2b). In the following discussion, we determine the electrochemically active area of the ceria nanoislands θ_{EC}^{Ce} [and the complementary electrochemically active area of clean Pt(111), $\theta_{EC}^{Pt} = 1 - \theta_{EC}^{Ce}$] from the attenuation of the OH adsorption/desorption peak on the HT and LT samples with respect to the reference CV of clean Pt(111), and the corresponding charge $q_{OH/Pt}^{ref}$ (Fig. S3, ESI†). θ_{EC}^{Ce} and θ_{EC}^{Pt} are evaluated as fractions of the clean Pt(111) surface.

(ii) The presence of ceria nanoislands does not have a pronounced effect on the H adsorption/desorption and $q_{H/Pt}$ in the CV of HT and LT samples, relative to the reference CV of clean Pt. This effect is clearly visible on LT samples (Fig. 2b), where the H adsorption/desorption peaks do not overlap with Ce^{3+}/Ce^{4+} redox peaks. This effect is apparent in HT samples as well (Fig. 2a), where the Ce^{3+}/Ce^{4+} redox peaks seem superimposed on the H adsorption/desorption region of clean Pt(111). In the following discussion, we assume $q_{H/Pt}$ to be constant for all HT and LT samples, and equal to $q_{H/Pt}^{ref}$ determined on clean Pt(111) (Fig. S3, ESI†).

(iii) The presence of ceria nanoislands does not influence significantly the double layer charge q_{DL}. In the CVs of HT samples, the double layer regions of HT samples show no or small broadening relative to clean Pt(111) (Fig. 2a, Fig. S7a–c, ESI†). For LT samples, the double layer region is occupied by broad Ce^{3+}/Ce^{4+} redox peaks (Fig. 2b, Fig. S7d–f, ESI†). For the 1.0 ML LT sample, it is however apparent that the double layer region is not significantly broadened compared to clean Pt(111) either (Fig. S7d, ESI†). Since q_{DL} is the smallest charge contribution, we assume q_{DL} to be constant for all HT and LT samples, and equal to q_{DL}^{ref} determined on clean Pt(111) (Fig. S3, ESI†).

Considering points (i)–(iii), the charge corresponding to Ce^{3+}/Ce^{4+} redox peaks in the HT and LT samples can be determined as $q_{Ce} = q_{tot}^{exp} - q_{DL}^{ref} - q_{H/Pt}^{ref} - (1 - \theta_{EC}^{Ce}){\cdot}q_{OH/Pt}^{ref}$, where q_{tot}^{exp} is the total charge experimentally determined in the CV of HT or LT samples, θ_{EC}^{Ce} is the electrochemically active area of the ceria nanoislands determined from the attenuation of the OH peak in the CV of the HT and LT samples, and q_{DL}^{ref}, $q_{H/Pt}^{ref}$, and $q_{OH/Pt}^{ref}$ are the reference charges determined for a clean Pt(111) surface. Determining q_{Ce} for HT and LT samples is illustrated graphically in Fig. 2c, d, and Fig. S7 (ESI†). A reference CV of clean Pt(111) and the corresponding scaling procedure to determine the attenuation of the OH peak are illustrated in Fig. S3 (ESI†).

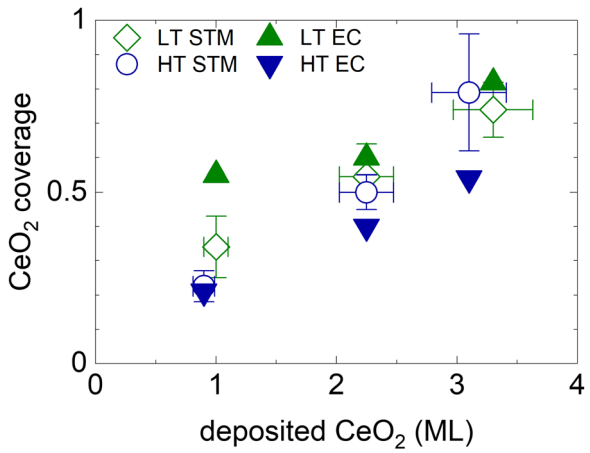

Fig. 4 Electrochemically active area of ceria nanoislands θ_{EC}^{Ce} in HT and LT samples (full symbols) in comparison with the coverage of CeO_2(111) nanoislands θ_{STM}^{Ce} estimated from STM images of the as-prepared samples shown in Fig. 1 and Table S1 (ESI†) (open symbols). The error bars represent the ±10% uncertainty in the amount of deposited CeO_2, and the upper and the lower estimates of CeO_2(111) STM coverage.

The electrochemically active CeO_2 area θ_{EC}^{Ce} for all HT and LT samples is shown in Fig. 4, and compared to the geometrical coverage of CeO_2 nanoislands θ_{STM}^{Ce} determined from STM images of the as-prepared samples (Fig. 1, Table S1, ESI†). θ_{EC}^{Ce} and θ_{STM}^{Ce} are plotted as a function of the amount of deposited CeO_2. We observe that θ_{STM}^{Ce} of both the HT and the LT samples, and θ_{EC}^{Ce} of HT samples scale linearly with the amount of CeO_2. θ_{EC}^{Ce} of LT samples is nonlinear with respect to the amount of CeO_2. θ_{EC}^{Ce} of the LT samples is also systematically higher than θ_{EC}^{Ce} of HT samples. These observations can be again assigned to the instability and redistribution of ceria nanoislands in LT samples during electrochemical cycling (Fig. 3b and Fig. S5e–h, ESI†), and, potentially, to the increase in volume of the nanoislands due to hydration of CeO_2 to $CeO_2 \cdot 2H_2O$. Another systematic trend can be observed in the θ_{EC}^{Ce} of HT samples. In spite of the electrochemical and morphological stability of the HT samples (Fig. 3a and Fig. S5a–d, ESI†), θ_{EC}^{Ce} is significantly lower than θ_{STM}^{Ce}. In this case, inhomogeneity of the samples represents the most likely explanation.

An evaluation of q_{Ce} and other charge contributions as a function of the amount of the deposited CeO_2 is shown in Fig. 5a for HT samples, and 5b for LT samples. q_{tot}^{exp} in all samples is, within ±10%, equal to q_{tot} on the clean Pt(111). The charge contribution q_{Ce} increases in all samples monotonically with the amount of deposited ceria. The HT samples show a smaller q_{Ce} value as compared to the LT samples. To estimate a bulk or a surface character of the Ce^{3+}/Ce^{4+} redox transition, we compare the evaluated q_{Ce} for HT and LT samples to the total charge density available for the Ce^{3+}/Ce^{4+} redox reaction in the bulk and on the surface of the as-prepared samples. The total charge density available for the Ce^{3+}/Ce^{4+} redox reaction in the bulk of the as-prepared samples is obtained as a product of Ce atom density in 1 ML of CeO_2(111) (7.9×10^{14} cm^{-2}), and the amount of deposited Ce, and it is indicated by the dashed line shown in Fig. 5a and b. Given the average thickness of ceria island (4 ± 1) ML for all as-prepared HT and LT samples (Table S1, ESI†), the total charge density available on the surface of the as-prepared samples is estimated as 1/4 of the

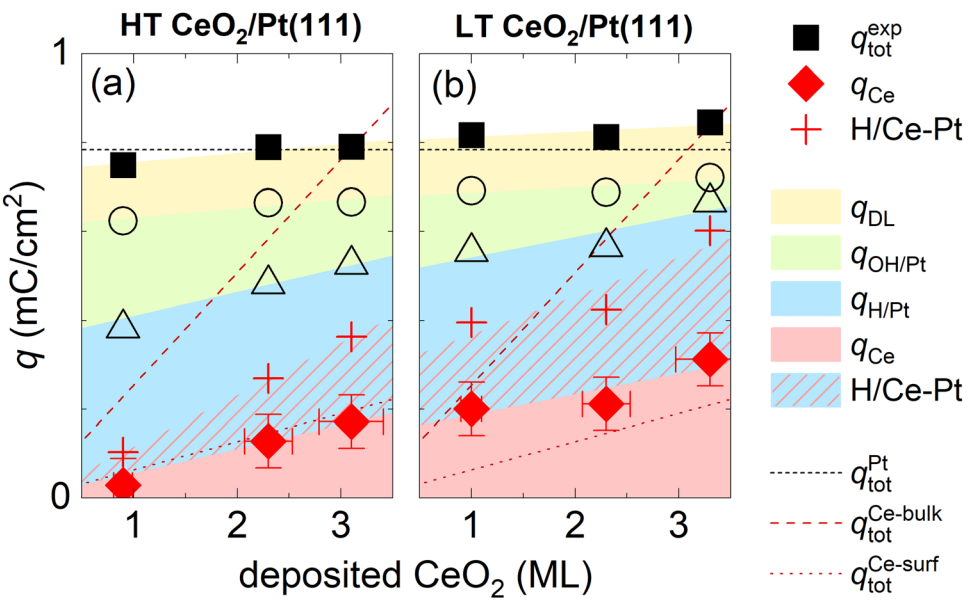

Fig. 5 Assignment of charge contributions in the CVs of HT and LT samples shown in Fig. 1 and 2 as a function of the amount of deposited CeO_2. Total charge in a CV (q_{tot}^{exp}), and the faradaic contribution to Ce^{3+}/Ce^{4+} electrooxidation/reduction (q_{Ce}) are marked with full symbols, incremental contributions to the total charge from H adsorption/desorption on Pt(111) ($q_{H/Pt}$), OH adsorption/desorption on Pt(111) ($q_{OH/Pt}$), and the double layer (q_{DL}) are marked with open symbols. The red crosses indicate the amount of H adsorbed/desorbed on Pt(111), which intercalates at the ceria/Pt interface (H/Ce-Pt). The color shading/hatching of the charge contributions represents a guide to the eyes. The dotted lines represent the total charge in the CV of clean Pt(111) (q_{tot}^{Pt}), and charge required for a complete oxidation/reduction of all deposited Ce atoms ($q_{tot}^{Ce\text{-}bulk}$) and surface Ce atoms ($q_{tot}^{Ce\text{-}surf}$).

charge density available in the bulk, and it is indicated by a dotted line shown in Fig. 5a and b. For HT samples, q_{Ce} corresponds well to the charge available at the surface of CeO_2(111), indicating the surface character of the Ce^{3+}/Ce^{4+} redox transition. For LT samples, the Ce^{3+}/Ce^{4+} redox transition involves more Ce atoms than originally available on the surface of the as-prepared LT samples. This indicates that the Ce^{3+}/Ce^{4+} redox transition in LT samples involves subsurface Ce atoms as well. These subsurface Ce atoms might have been exposed during redistribution of the as-prepared CeO_2 nanoislands in LT samples.

Hydrogen intercalation at the ceria–Pt interface

CVs of ceria nanoislands in both the HT and the LT samples presented in this study differ qualitatively from CVs reported previously for transition metal inverse model catalysts, *i.e.* nanoislands of transition metal oxyhydroxides on Pt(111).[54,55] Particularly, in contrast to ceria nanoislands, transition metal oxyhydroxide nanoislands on Pt(111) block both the OH adsorption/desorption and H adsorption/desorption on Pt(111).[54,55] This different behavior is also reproduced in our experimental setup. Transition metal ions represent a trace contaminant in commercial ultrapure KOH, and the deposition of transition metal oxyhydroxide nanoparticles can be observed on Pt(111) upon extended electrochemical cycling.[56] The CV of Pt(111) upon such extended cycling is displayed in Fig. S8 (ESI†). The CV shows peaks assigned to transition metal oxyhydroxides, and the corresponding attenuation of both OH adsorption/desorption and H adsorption/desorption on Pt(111).[56]

To explain this somewhat counterintuitive behavior of ceria nanoislands, *i.e.* our observation that H adsorption/desorption on Pt(111) remains apparently unchanged even in cases when OH adsorption/desorption is significantly attenuated for the HT and LT samples (Fig. 2a, b and Fig. S7, ESI†), we must invoke a fast and reversible reaction removing the adsorbed H atoms from the free Pt(111) surface in the cathodic scan, and replenishing them back on Pt(111) in the anodic scan. We may estimate the amount of adsorbed H atoms that must take part in this reaction as $\theta_{EC}^{Ce} \cdot q_{H/Pt}^{ref}$. This amount is indicated in Fig. 5a and b using red crosses. We propose that the adsorbed H atoms are removed from Pt(111) by surface diffusion and intercalated at the Pt/ceria interface. Such non-faradaic process involves no charge transfer between H atoms and the working electrode, and, consequently, no additional features in the CV. Intercalated H atoms still interact with the Pt(111) substrate, which limits the charge of H adsorbed on Pt(111) in HT and LT samples to 2/3 of the density of Pt(111) surface atoms,[15] as is the case for clean Pt(111).

We note that the intercalated atomic hydrogen may eventually further react with ceria. Some reaction pathways were previously identified in hydrogen reactions with ceria, particularly the creation of O–H bonds followed by reduction of Ce^{4+} to Ce^{3+} as observed for nearly stoichiometric samples of cubic ceria,[31] and creation of Ce–H bonds followed by oxidation of Ce^{3+} to Ce^{4+} as observed for reduced ceria containing high concentration of oxygen vacancies.[57–59] Such non-faradaic reactions may be the cause for the irreversible nature and asymmetry of Ce^{3+}/Ce^{4+} redox peaks in the CV curves of the HT and LT samples (Fig. 2). Identification and analysis of the involved ceria phases are however beyond the scope of this manuscript.

Suppressing the onset of the HER reaction

In spite of the fact that due to H intercalation, ceria/Pt model electrocatalysts can accommodate an amount of adsorbed H which is comparable to that of a clean Pt(111) surface, the presence of ceria nanoislands suppresses the onset of the hydrogen evolution reaction for the HT and the LT samples. The onset of the HER in the CVs shown in Fig. 2 is summarized in Fig. S9 (ESI†). For all HT and LT samples, the onset of the HER is suppressed in comparison with the clean Pt(111) surface. In LT samples, suppression of the HER onset gets stronger with increasing ceria coverage. In the first approximation, the suppressed onset of the HER observed on our model ceria/Pt samples can be interpreted as a geometrical effect with the HER proceeding only on the fraction of Pt(111) exposed to the electrolyte, and with no participation of H intercalated at the ceria surface. In the case of a continuous ceria layer on Pt(111), and at potentials investigated in this study (Fig. S4, ESI†), no HER is observed at all.

Conclusions

We identified structure–property relationships and bifunctional electrocatalytic mechanisms in a rare-earth oxide-based model electrocatalyst, *i.e.* CeO_2(111)/Pt(111). We used a model electrocatalytic approach with the catalysts prepared and characterized by experimental techniques of surface science (physical vapor deposition, STM, AFM, XPS, LEED). The structural and chemical properties of the model catalysts were then correlated to electrochemical properties investigated *via* cyclic voltammetry in alkaline electrolyte (CV, 0.1 M KOH).

Stability and redox properties

Flat and compact CeO_2(111) nanoislands with lateral sizes of approx. 20 nm or larger, and straight edges are stable during cycling at potentials between −0.05 and 0.9 V_{RHE}. The CV peaks assigned to the electrooxidation/electroreduction of surface Ce atoms are irreversible and appear at approx. 0.15/0.30 V_{RHE} (cathodic/anodic scan). Similar peaks are identified for a continuous CeO_2(111) layer on Pt(111). The peaks are assigned to $CeO_2 \rightleftharpoons Ce(OH)_3$ transition.

Flat and open CeO_2(111) nanoislands with lateral sizes below approx. 5 nm, and with rounded edges are initially unstable. The CV peaks assigned to the electrooxidation/electroreduction of surface and subsurface Ce atoms are irreversible and stabilize at higher potentials of approx. 0.45/0.70 V_{RHE} (cathodic/anodic scan). This observation is interpreted as a phase change of ceria nanoislands from cubic CeO_2 to

amorphous ceria hydrate $CeO_2{\cdot}2H_2O$, and the shifted irreversible peaks assigned to the $CeO_2{\cdot}2H_2O \rightleftharpoons Ce(OH)_3$ transition.

Large *vs.* small $CeO_2(111)$ nanoislands were prepared using different preparation methods, but their stability/instability in CV is interpreted as a predominantly structural effect. The small $CeO_2(111)$ nanoislands include a substantial fraction of undercoordinated surface sites (oxygen vacancies, kink sites at rounded edges) as compared to the larger and compact nanoislands. Upon potential cycling, these undercoordinated sites react with H_2O to yield a hydrated $CeO_2{\cdot}2H_2O$ phase. Both CeO_2 and $CeO_2{\cdot}2H_2O$ nanoislands, which appear at oxidizing potentials (above 0.3 and 0.7 V_{RHE}, respectively), are reduced at lower potentials (0.15 and 0.45 V_{RHE}, respectively), resulting in the creation of Ce^{3+} containing inhomogeneous and partly hydroxylated phases that can be denoted as cerium oxyhydroxide.

Bifunctionality and hydrogen intercalation

Quantitative analysis of the charge in the CVs for the transformation of $CeO_2(111)$ and $CeO_2{\cdot}2H_2O$ nanoislands on Pt(111) reveals a bifunctional mechanism in which a fraction of H atoms adsorbed on Pt(111) undergoes surface diffusion and intercalation at the Pt/ceria interface. This non-faradaic mechanism is reversible and allows the accommodation of H atoms on the whole Pt(111) surface in spite of the fact that part of the Pt is occupied by $CeO_2(111)$ or $CeO_2{\cdot}2H_2O$. This behavior is contrary to what is observed in the case of nanoislands of transition metal oxyhydroxides on Pt(111), which tend to block the adsorption/desorption of H. H accommodated at the Pt/ceria interface likely contributes to establishing cerium oxyhydroxide phases at reducing potentials, but it cannot participate in the HER on ceria/Pt model catalysts.

Outlook

Our investigations illustrate the power of model electrocatalyst studies in identifying the conditions and consequences of physicochemical and electrochemical processes relevant to metal-oxide electrocatalysis. The redox properties of the ceria/Pt(111) model system in the electrochemical environment are complex and involve the formation of different cerium phases which can be partly controlled *via* preparation procedures and the applied potential. The present identification of the cerium phases established under electrochemical conditions may contribute to understanding and knowledge-based improvement of technologically favorable properties of ceria-based electrocatalysts.

Data availability

Original experimental data are available *via* Zenodo, DOI: **https://doi.org/10.5281/zenodo.8231965**.

Conflicts of interest

There are no conflicts to declare.

Acknowledgements

The authors acknowledge financial support from the Czech Science Foundation (project GAČR 20-11688J) and the Deutsche Forschungsgemeinschaft (DFG) (project 431733372). Support from the DFG *via* Collaborative Research Centre SFB 1452 – Catalysis at Liquid Interfaces (project 431791331), and project 453560721 is acknowledged. P. K. S. thanks the Grant Agency of the Charles University for the support (project GAUK 326122).

References

1 L. Liu and A. Corma, Structural Transformations of Solid Electrocatalysts and Photocatalysts, *Nat. Rev. Chem.*, 2021, **5**, 256.
2 S. Zhao, Y. Yang and Z. Tang, Insight into Structural Evolution, Active Sites, and Stability of Heterogeneous Electrocatalysts, *Angew. Chem., Int. Ed.*, 2022, **61**, e202110186.
3 K. Fan, H. Zou, Y. Lu, H. Chen, F. Li, J. Liu, L. Sun, L. Tong, M. F. Toney and M. Sui, *et al.*, Direct Observation of Structural Evolution of Metal Chalcogenide in Electrocatalytic Water Oxidation, *ACS Nano*, 2018, **12**, 12369.
4 H.-Y. Wang, S.-F. Hung, H.-Y. Chen, T.-S. Chan, H. M. Chen and B. Liu, In Operando Identification of Geometrical-Site-Dependent Water Oxidation Activity of Spinel Co_3O_4, *J. Am. Chem. Soc.*, 2016, **138**, 36.
5 M. Favaro, J. Yang, S. Nappini, E. Magnano, F. M. Toma, E. J. Crumlin, J. Yano and I. D. Sharp, Understanding the Oxygen Evolution Reaction Mechanism on CoO_x Using Operando Ambient-Pressure X-Ray Photoelectron Spectroscopy, *J. Am. Chem. Soc.*, 2017, **139**, 8960.
6 Y. Duan, J. Y. Lee, S. Xi, Y. Sun, J. Ge, S. J. H. Ong, Y. Chen, S. Dou, F. Meng and C. Diao, *et al.*, Anodic Oxidation Enabled Cation Leaching for Promoting Surface Reconstruction in Water Oxidation, *Angew. Chem., Int. Ed.*, 2021, **60**, 7418.
7 S. Song, L. Mu, Y. Jiang, J. Sun, Y. Zhang, G. Shi and H. Sun, Turning Electrocatalytic Activity Sites for the Oxygen Evolution Reaction on Brownmillerite to Oxyhydroxide, *ACS Appl. Mater. Interfaces*, 2022, **14**, 47560.
8 F. Dionigi, Z. Zeng, I. Sinev, T. Merzdorf, S. Deshpande, M. B. Lopez, S. Kunze, I. Zegkinoglou, H. Sarodnik and D. Fan, *et al.*, In-Situ Structure and Catalytic Mechanism of NiFe and CoFe Layered Double Hydroxides during Oxygen Evolution, *Nat. Commun.*, 2020, **11**, 2522.
9 J. Huang, Y. Li, Y. Zhang, G. Rao, C. Wu, Y. Hu, X. Wang, R. Lu, Y. Li and J. Xiong, Identification of Key Reversible Intermediates in Self-Reconstructed Nickel-Based Hybrid Electrocatalysts for Oxygen Evolution, *Angew. Chem., Int. Ed.*, 2019, **58**, 17458.
10 L. Gao, X. Cui, C. D. Sewell, J. Li and Z. Lin, Recent Advances in Activating Surface Reconstruction for the High-Efficiency Oxygen Evolution Reaction, *Chem. Soc. Rev.*, 2021, **50**, 8428.
11 N. Danilovic, R. Subbaraman, D. Strmcnik, K. Chang, A. P. Paulikas, V. R. Stamenkovic and N. M. Markovic, Enhancing the Alkaline Hydrogen Evolution Reaction

Activity through the Bifunctionality of $Ni(OH)_2$/Metal Catalysts, *Angew. Chem., Int. Ed.*, 2012, **51**, 12495.

12 W. Huang, H. Wang, J. Zhou, J. Wang, P. N. Duchesne, D. Muir, P. Zhang, N. Han, F. Zhao and M. Zeng, *et al.*, Highly Active and Durable Methanol Oxidation Electrocatalyst Based on the Synergy of Platinum–Nickel Hydroxide–Graphene, *Nat. Commun.*, 2015, **6**, 10035.

13 D. Y. Chung, P. P. Lopes, P. Farinazzo Bergamo Dias Martins, H. He, T. Kawaguchi, P. Zapol, H. You, D. Tripkovic, D. Strmcnik and Y. Zhu, *et al.*, Dynamic Stability of Active Sites in Hydr(Oxy)Oxides for the Oxygen Evolution Reaction, *Nat. Energy*, 2020, **5**, 222.

14 D. M. Kolb, Electrochemical Surface Science, *Angew. Chem., Int. Ed.*, 2001, **40**, 1162.

15 N. M. Markovic and P. N. J. Ross, Surface Science Studies of Model Fuel Cell Electrocatalysts, *Surf. Sci. Rep.*, 2002, **45**, 117.

16 F. Faisal, C. Stumm, M. Bertram, F. Waidhas, Y. Lykhach, S. Cherevko, F. Xiang, M. Ammon, M. Vorokhta and B. Šmíd, *et al.*, Electrifying Model Catalysts for Understanding Electrocatalytic Reactions in Liquid Electrolytes, *Nat. Mater.*, 2018, **17**, 592.

17 A. R. Akbashev, Electrocatalysis Goes Nuts, *ACS Catal.*, 2022, **12**, 4296.

18 O. Brummel, Y. Lykhach, M. Ralaiarisoa, M. Berasategui, M. Kastenmeier, L. Fusek, A. Simanenko, W. Gu, P. C. J. Clark and R. Yivlialin, *et al.*, A Versatile Approach to Electrochemical In Situ Ambient-Pressure X-Ray Photoelectron Spectroscopy: Application to a Complex Model Catalyst, *J. Phys. Chem. Lett.*, 2022, **13**, 11015.

19 J. Fester, A. Makoveev, D. Grumelli, R. Gutzler, Z. Sun, J. Rodríguez-Fernández, K. Kern and J. V. Lauritsen, The Structure of the Cobalt Oxide/Au Catalyst Interface in Electrochemical Water Splitting, *Angew. Chem., Int. Ed.*, 2018, **57**, 11893.

20 F. Reikowski, F. Maroun, I. Pacheco, T. Wiegmann, P. Allongue, J. Stettner and O. M. Magnussen, Operando Surface X-Ray Diffraction Studies of Structurally Defined Co_3O_4 and CoOOH Thin Films during Oxygen Evolution, *ACS Catal.*, 2019, **9**, 3811.

21 T. Wiegmann, I. Pacheco, F. Reikowski, J. Stettner, C. Qiu, M. Bouvier, M. Bertram, F. Faisal, O. Brummel and J. Libuda, *et al.*, Operando Identification of the Reversible Skin Layer on Co_3O_4 as a Three-Dimensional Reaction Zone for Oxygen Evolution, *ACS Catal.*, 2022, **12**, 3256.

22 C. Stumm, M. Bertram, M. Kastenmeier, F. D. Speck, Z. Sun, J. Rodríguez-Fernández, J. V. Lauritsen, K. J. J. Mayrhofer, S. Cherevko and O. Brummel, *et al.*, Structural Dynamics of Ultrathin Cobalt Oxide Nanoislands under Potential Control, *Adv. Funct. Mater.*, 2021, **31**, 2009923.

23 D. Grumelli, T. Wiegmann, S. Barja, F. Reikowski, F. Maroun, P. Allongue, J. Balajka, G. S. Parkinson, U. Diebold and K. Kern, *et al.*, Electrochemical Stability of the Reconstructed Fe_3O_4(001) Surface, *Angew. Chem., Int. Ed.*, 2020, **59**, 21904.

24 M. Müllner, M. Riva, F. Kraushofer, M. Schmid, G. S. Parkinson, S. F. L. Mertens and U. Diebold, Stability and Catalytic Performance of Reconstructed Fe_3O_4(001) and Fe_3O_4(110) Surfaces during Oxygen Evolution Reaction, *J. Phys. Chem. C*, 2019, **123**, 8304.

25 M. Bertram, C. Prössl, M. Ronovský, J. Knöppel, P. Matvija, L. Fusek, T. Skála, N. Tsud, M. Kastenmeier and V. Matolín, *et al.*, Cobalt Oxide-Supported Pt Electrocatalysts: Intimate Correlation between Particle Size, Electronic Metal–Support Interaction and Stability, *J. Phys. Chem. Lett.*, 2020, **11**, 8365.

26 F. Buchner, M. Eckardt, T. Böhler, J. Kim, J. Gerlach, J. Schnaidt and R. J. Behm, Oxygen Reduction and Evolution on Ni-modified Co_3O_4(111) Cathodes for Zn–Air Batteries: A Combined Surface Science and Electrochemical Model Study, *ChemSusChem*, 2020, **13**, 3199.

27 F. Buchner, S. Fuchs and R. J. Behm, UHV Preparation and Electrochemical/-Catalytic Properties of Well-Defined Co– and Fe-Containing Unary and Binary Oxide Model Cathodes for the Oxygen Reduction and Oxygen Evolution Reaction in Zn-Air Batteries, *J. Electroanal. Chem.*, 2021, **896**, 115497.

28 Z. Sun, A. Curto, J. Rodríguez-Fernández, Z. Wang, A. Parikh, J. Fester, M. Dong, A. Vojvodic and J. V. Lauritsen, The Effect of Fe Dopant Location in $Co(Fe)OOH_x$ Nanoparticles for the Oxygen Evolution Reaction, *ACS Nano*, 2021, **15**, 18226.

29 D. R. Kauffman, X. Deng, D. C. Sorescu, T.-D. Nguyen-Phan, C. Wang, C. M. Marin, E. Stavitski, I. Waluyo and A. Hunt, Edge-Enhanced Oxygen Evolution Reactivity at Ultrathin, Au-Supported Fe_2O_3 Electrocatalysts, *ACS Catal.*, 2019, **9**, 5375.

30 A. Trovarelli and P. Fornasiero, *Catalysis by Ceria and Related Materials*, 2nd edn, World Scientific, Singapore, 2013.

31 D. R. Mullins, The Surface Chemistry of Cerium Oxide, *Surf. Sci. Rep.*, 2015, **70**, 42.

32 J. Corchado-García, L. E. Betancourt, C. A. Vélez, S. D. Senanayake, D. Stacchiola, K. Sasaki, M. J.-F. Guinel, Y. Zhou, C. L. Cheung and C. R. Cabrera, Cerium Oxide as a Promoter for the Electro-Oxidation Reaction of Ethanol: In Situ XAFS Characterization of the Pt Nanoparticles Supported on CeO_2 Nanoparticles and Nanorods, *Phys. Chem. Chem. Phys.*, 2015, **17**, 32251.

33 Y. Katayama, T. Okanishi, H. Muroyama, T. Matsui and K. Eguchi, Enhanced Supply of Hydroxyl Species in CeO_2-Modified Platinum Catalyst Studied by in Situ ATR-FTIR Spectroscopy, *ACS Catal.*, 2016, **6**, 2026.

34 O. Brummel, F. Waidhas, F. Faisal, R. Fiala, M. Vorokhta, I. Khalakhan, M. Dubau, A. Figueroba, G. Kovács and H. A. Aleksandrov, *et al.*, Stabilization of Small Platinum Nanoparticles on Pt–CeO_2 Thin Film Electrocatalysts During Methanol Oxidation, *J. Phys. Chem. C*, 2016, **120**, 19723.

35 Z. Weng, W. Liu, L.-C. Yin, R. Fang, M. Li, E. I. Altman, Q. Fan, F. Li, H.-M. Cheng and H. Wang, Metal/Oxide Interface Nanostructures Generated by Surface Segregation for Electrocatalysis, *Nano Lett.*, 2015, **15**, 7704.

36 K. R. Yoon, J. M. Kim, K. A. Lee, C.-K. Hwang, S. G. Akpe, Y. J. Lee, J. P. Singh, K. H. Chae, S. S. Jang and H. C. Ham, *et al.*, Activity-Stability Benefits of Pt/C Fuel Cell

Electrocatalysts Prepared via Remote CeO_2 Interfacial Doping, *J. Power Sources*, 2021, **496**, 229798.

37 K. Fugane, T. Mori, D. R. Ou, P. Yan, F. Ye, H. Yoshikawa and J. Drennan, Improvement of Cathode Performance on Pt-CeO_x by Optimization of Electrochemical Pretreatment Condition for PEFC Application, *Langmuir*, 2012, **28**, 16692.

38 S. Chauhan, T. Mori, T. Masuda, S. Ueda, G. J. Richards, J. P. Hill, K. Ariga, N. Isaka, G. Auchterlonie and J. Drennan, Design of Low Pt Concentration Electrocatalyst Surfaces with High Oxygen Reduction Reaction Activity Promoted by Formation of a Heterogeneous Interface between Pt and CeO_x Nanowire, *ACS Appl. Mater. Interfaces*, 2016, **8**, 9059.

39 M. Liu, K. Min, B. Han and L. Y. S. Lee, Interfacing or Doping? Role of Ce in Highly Promoted Water Oxidation of NiFe-Layered Double Hydroxide, *Adv. Energy Mater.*, 2021, **11**, 2101281.

40 P. Luches, F. Pagliuca and S. Valeri, Morphology, Stoichiometry, and Interface Structure of CeO_2 Ultrathin Films on Pt(111), *J. Phys. Chem. C*, 2011, **115**, 10718.

41 P. Luches, F. Pagliuca and S. Valeri, Structural and Morphological Modifications in Thermally Reduced Cerium Oxide Ultrathin Epitaxial Films on Pt(111), *Phys. Chem. Chem. Phys.*, 2014, **16**, 18848.

42 T. V. Plakhova, A. Y. Romanchuk, S. N. Yakunin, T. Dumas, S. Demir, S. Wang, S. G. Minasian, D. K. Shuh, T. Tyliszczak and A. A. Shiryaev, *et al.*, Solubility of Nanocrystalline Cerium Dioxide: Experimental Data and Thermodynamic Modeling, *J. Phys. Chem. C*, 2016, **120**, 22615.

43 P. Yu, S. A. Hayes, T. J. O'Keefe, M. J. O'Keefe and J. O. Stoffer, The Phase Stability of Cerium Species in Aqueous Systems, *J. Electrochem. Soc.*, 2006, **153**, C74.

44 T. Duchoň, F. Dvořák, M. Aulická, V. Stetsovych, M. Vorokhta, D. Mazur, K. Veltruská, T. Skála, J. Mysliveček and I. Matolínová, *et al.*, Ordered Phases of Reduced Ceria As Epitaxial Films on Cu(111), *J. Phys. Chem. C*, 2014, **118**, 357.

45 C. J. Neal, T. S. Sakthivel, Y. Fu and S. Seal, Aging of Nanoscale Cerium Oxide in a Peroxide Environment: Its Influence on the Redox, Surface, and Dispersion Character, *J. Phys. Chem. C*, 2021, **125**, 27323.

46 E. A. Kümmerle and G. Heger, The Structures of C–$Ce_2O_{3+\delta}$, Ce_7O_{12}, and $Ce_{11}O_{20}$, *J. Solid State Chem.*, 1999, **147**, 485.

47 D. Schweke, G. Rafailov, S. Zalkind, O. Azulai, L. Rabinovitch and S. Hayun, Elucidating the Role of Hydrogen Species Originating from Water Vapor in the Oxidation Mechanism of Cerium, *Corros. Sci.*, 2022, **196**, 110030.

48 D. Schweke, A. Rubin, L. Rabinovitch, O. Kraynis and T. Livneh, Cerium Metal Oxidation Studied by IR Reflection-Absorption and Raman Scattering Spectroscopies, *J. Phys.: Condens. Matter*, 2022, **34**, 324002.

49 F. Dvořák, L. Szabová, V. Johánek, M. Farnesi Camellone, V. Stetsovych, M. Vorokhta, A. Tovt, T. Skála, I. Matolínová and Y. Tateyama, *et al.*, Bulk Hydroxylation and Effective Water Splitting by Highly Reduced Cerium Oxide: The Role of O Vacancy Coordination, *ACS Catal.*, 2018, **8**, 4354.

50 P. Abellan, T. H. Moser, I. T. Lucas, J. W. Grate, J. E. Evans and N. D. Browning, The Formation of Cerium(III) Hydroxide Nanoparticles by a Radiation Mediated Increase in Local pH, *RSC Adv.*, 2017, **7**, 3831.

51 B. Djuričić and S. Pickering, Nanostructured Cerium Oxide: Preparation and Properties of Weakly-Agglomerated Powders, *J. Eur. Ceram. Soc.*, 1999, **19**, 1925.

52 S. V. N. T. Kuchibhatla, A. S. Karakoti, A. E. Vasdekis, C. F. Windisch, S. Seal, S. Thevuthasan and D. R. Baer, An Unexpected Phase Transformation of Ceria Nanoparticles in Aqueous Media, *J. Mater. Res.*, 2019, **34**, 465.

53 U. Lavrencic Stangar, B. Orel, I. Grabec and B. Ogorvec, Optical and Electrochemical Properties of CeO_2 and CeO_2-TiO_2 Coatings, *Solar Energy Materials and Solar Cells*, 1993, **31**, 171.

54 R. Subbaraman, D. Tripkovic, D. Strmcnik, K.-C. Chang and M. Uchimura, Paulikas, a P.; Stamenkovic, V.; Markovic, N. M. Enhancing Hydrogen Evolution Activity in Water Splitting by Tailoring Li^+-$Ni(OH)_2$-Pt Interfaces, *Science*, 2011, **334**, 1256.

55 R. Subbaraman, D. Tripkovic, K.-C. Chang, D. Strmcnik, A. P. Paulikas, P. Hirunsit, M. Chan, J. Greeley, V. Stamenkovic and N. M. Markovic, Trends in Activity for the Water Electrolyser Reactions on 3d M(Ni,Co,Fe,Mn) Hydr(Oxy)Oxide Catalysts, *Nat. Mater.*, 2012, **11**, 550.

56 R. Subbaraman, N. Danilovic, P. P. Lopes, D. Tripkovic, D. Strmcnik, V. R. Stamenkovic and N. M. Markovic, Origin of Anomalous Activities for Electrocatalysts in Alkaline Electrolytes, *J. Phys. Chem. C*, 2012, **116**, 22231.

57 Z. Li, K. Werner, K. Qian, R. You, A. Płucienik, A. Jia, L. Wu, L. Zhang, H. Pan and H. Kuhlenbeck, *et al.*, Oxidation of Reduced Ceria by Incorporation of Hydrogen, *Angew. Chem., Int. Ed.*, 2019, **58**, 14686.

58 Z. Li, K. Werner, L. Chen, A. Jia, K. Qian, J. Zhong, R. You, L. Wu, L. Zhang and H. Pan, *et al.*, Interaction of Hydrogen with Ceria: Hydroxylation, Reduction, and Hydride Formation on the Surface and in the Bulk, *Chem. – Eur. J.*, 2021, **27**, 5268.

59 T. Matsukawa, K. Iida, M. Nakamura and T. Ishigaki, Detection of Hydroxyl and Hydride Functional Groups in a Ceria Crystal under Hydrogen Reduction, *CrystEngComm*, 2021, **23**, 2355.